LAWRENCE
LIVERMORE
NATIONAL
LABORATORY

UCRL-PROC-233897

Amplitude variations on the Extreme Adaptive Optics testbed

Julia Evans, Sandrine Thomas, Daren Dillon, Donald Gavel, Donald Phillion, Bruce Macintosh

August 22, 2007

SPIE Optics and Photonics
San Diego, CA, United States
August 26, 2007 through August 30, 2007

Disclaimer

This document was prepared as an account of work sponsored by an agency of the United States Government. Neither the United States Government nor the University of California nor any of their employees, makes any warranty, express or implied, or assumes any legal liability or responsibility for the accuracy, completeness, or usefulness of any information, apparatus, product, or process disclosed, or represents that its use would not infringe privately owned rights. Reference herein to any specific commercial product, process, or service by trade name, trademark, manufacturer, or otherwise, does not necessarily constitute or imply its endorsement, recommendation, or favoring by the United States Government or the University of California. The views and opinions of authors expressed herein do not necessarily state or reflect those of the United States Government or the University of California, and shall not be used for advertising or product endorsement purposes.

Amplitude variations on the ExAO testbed

Julia W. Evans[a], Sandrine Thomas[b], Daren Dillon[b], Donald Gavel[b], Donald Phillion[a], Bruce Macintosh[a,b]

[a]Lawrence Livermore National Laboratory, 7000 East Avenue, Livermore,USA
[b]UCO Lick Observatory, Laboratory for Adaptive Optics, University of California at Santa Cruz, 1156 High St., Santa Cruz, CA, 95064

ABSTRACT

High-contrast adaptive optics systems, such as those needed to image extrasolar planets, are known to require excellent wavefront control and diffraction suppression. At the Laboratory for Adaptive Optics on the Extreme Adaptive Optics testbed, we have already demonstrated wavefront control of better than 1 nm rms within controllable spatial frequencies. Corresponding contrast measurements, however, are limited by amplitude variations, including those introduced by the micro-electrical-mechanical-systems (MEMS) deformable mirror. Results from experimental measurements and wave optic simulations of amplitude variations on the ExAO testbed are presented. We find systematic intensity variations of about 2% rms, and intensity variations with the MEMS to be 6%. Some errors are introduced by phase and amplitude mixing because the MEMS is not conjugate to the pupil, but independent measurements of MEMS reflectivity suggest that some error is introduced by small non-uniformities in the reflectivity.

Keywords: Adaptive Optics, MEMS, Extreme Adaptive Optics

1. INTRODUCTION

High-contrast imaging, of the type required to image exoplanets, is both technically challenging and a growing area of research. The technical challenges are being explored by many groups in support of future planet imagers. Our work on the ExAO testbed in the Laboratory for Adaptive Optics (LAO) at UC Santa Cruz supports the Gemini Planet Imager (GPI),[1] which has expected first light in 2010. The SPHERE project also has a ground-based imager under development planned for first light in the same year.[2] Both ground-based imagers hope to achieve contrast of between 10^{-6} and 10^{-7} in order to image young Jupiter-like planets. The Terrestrial Planet Finder (TPF) is a space-based instrument with more stringent contrast requirements for imaging earth-like planets. Testbed experiments in support of TPF are on-going on the High Contrast Imaging Testbed (HCIT).[3]

It is well known that high-contrast imaging requires excellent diffraction suppression and low wavefront errors. It is becoming clear that amplitude errors must also be considered, either in design choices or with active control. Previous work at the LAO includes demonstrating 6.5×10^{-8} contrast from 10 to 25 λ/D without active phase control using a prolate shaped pupil for diffraction suppression.[4] In that case contrast was limited by wavefront error. After extensive testing of 1024-actuator micro-electrical-mechanical-systems (MEMS) deformable mirrors (DMs) we achieved precision phase control of better than 1 nm rms over a 9.2 mm aperture within the controllable spatial frequencies of the DM.[5] The obvious next step is to measure contrast with active phase control. These measurements have been done and preliminary results presented previously,[6] however as discussed in Section 3 contrast measurements with the MEMS deformable mirrors are more complicated than with the flat mirror. One such complication are the increased amplitude variations for the system with the MEMS DM compared to with a flat mirror. In this paper we present our investigation into the magnitude, sources and effect of amplitude variation on far-field contrast for the ExAO testbed. Because of their more stringent contrast requirements HCIT completed a full investigation of amplitude variation including an end-to-end system simulation and experimental measurements.[7] They found amplitude errors to limit contrast to 10^{-6} levels and active amplitude correction in the form of speckle nulling was used to correct those limiting errors over a half dark hole region[3] allowing contrasts of 6×10^{-10}.

2. EXPERIMENTAL METHOD

The original layout for the ExAO testbed is described in several publications.[4,5] In brief the simple design had low wavefront error (< 1.5 nm rms), but was limited to one pupil plane (about 18 cm in front of the MEMS DM) and one focal plane. The built in metrology of the phase shifting diffraction interferometer (PSDI)[8] allowed excellent wavefront characterization to compliment far-field contrast measurements, but diffraction was suppressed with a shaped pupil producing only a small high-contrast region. A beam splitter and spatially filtered wavefront sensor were added to the system.[9] Phase II was completed in 2006 and extends the Phase I system with two spherical mirrors to add an additional pupil and focal plane, allowing a more sophisticated lyot-style coronagraph to be used to suppress diffraction. A pupil imaging mode can be used for characterizing amplitude errors. The pupil is still not quite conjugate to the DM which introduces some errors that will be discussed later.

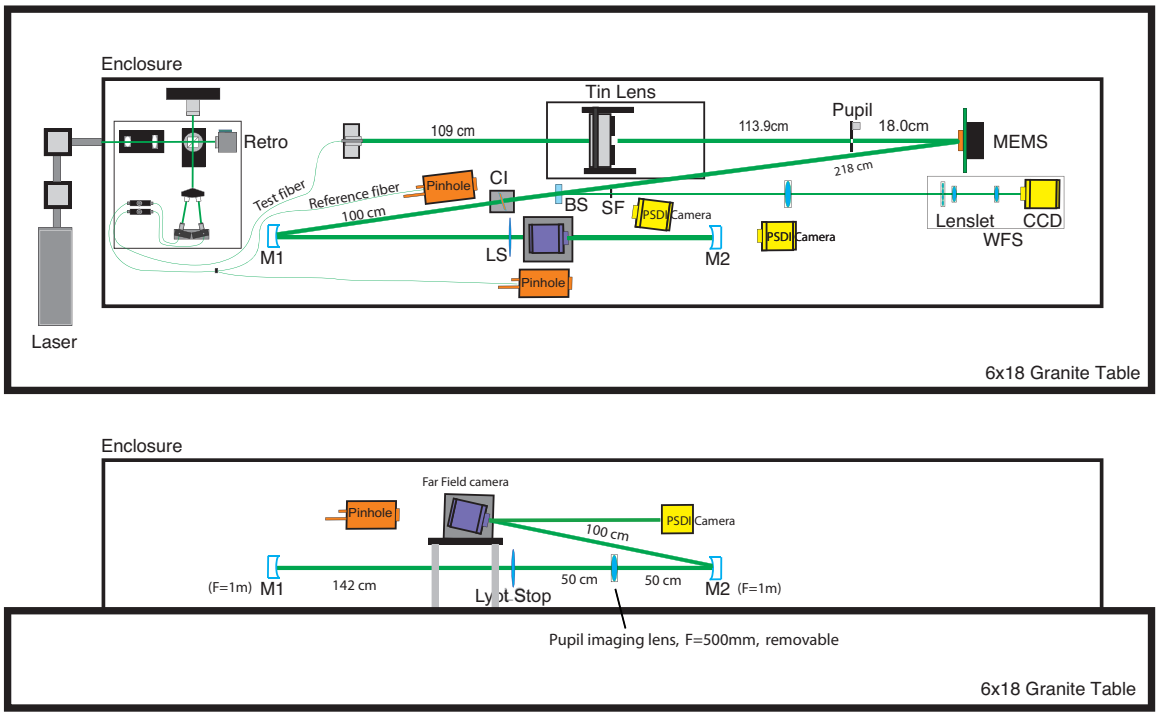

Figure 1. Schematic of the Phase II ExAO testbed. The PSDI front end located at the top left feeds the test (measurement) and reference fibers for the system. The PSDI pinhole can be placed at focus position 1 (labeled CI for coronagraph input), effectively reproducing the phase I system or by replacing the far-field CCD the pinhole can be placed at focus position 2. The far-field camera is out-of-plane to reduce astigmatism introduced by the spherical mirrors (M1 and M2).

Figure 1 is a schematic of the Phase II testbed. In the top left corner is the PSDI front end which feeds both the reference and the measurement (or test) beams. The pinhole can be placed at focus position one, labeled CI for coronagraph input, or can replace the far-field camera at focus position 2. Putting the pinhole at focus position 1 effectively replicates the Phase I testbed. The two spherical mirrors used to re-image the pupil introduce astigmatism, and the far-field camera is placed out-of-plane to correct that error. A pupil imaging lens can be placed after the Lyot stop (second pupil plan) to re-image the pupil onto the far-field CCD. This is the pupil imaging mode. Astigmatism is not as well corrected in the pupil imaging mode leading to an additional

error source on the order of 20 nm rms in this mode. The beam splitter (BS) before the first focus feeds the spatial filtered (SF) Shack-Hartman wavefront sensor (WFS), which was not used for the results presented here. The deformable mirror is a 1024 - actuator MEMS DM, produced by Boston Micromachines.

2.1 Simulations

Amplitude variations can be introduced by real intensity variations caused by non-uniform illumination or coating imperfections in optics, but they can also be introduced by wave optic effects, like phase and amplitude mixing.[7,10] Wave optic effects might be misinterpreted by the instrumentation we use for measuring amplitude variation, further confusing the results. Wave-optic simulations can provide insight into understanding and identification of wave optic induced amplitude variation.

The PSDI uses a wave optics propagation program for 'lensless imaging' of the pupil or MEMS planes. The program is called Stitch and it can also be used to simulate the effect of amplitude or phase variations introduced in the pupil or MEMS planes.[11] The code is used during normal operation of the PSDI. The interference pattern generated by the reference and measurement (test) beams is recorded at a CCD located in an arbitrary location along the optical axis. Using standard phase-shifting interferometer techniques this produces a measurement of the fringe pattern at this location, which can then be converted to a wavefront. This wavefront is numerically propagated using Stitch in two steps to the plane of interest using the ABCD matrix and a Huygens Integral transformation implemented with FFTs. For simulation purposes an initial wavefront is generated at the plane of interest then the code propagates the input phase and amplitude to focus and then to the PSDI CCD position. With the wavefront now measured at the CCD position the typical back propagation is used to return to the pupil or MEMS plane. This simulation reflects the phase I configuration of the system quite well, and as the PSDI code was tested extensively during its development[8] it is a powerful tool for understanding amplitude and phase errors. Stich is not very flexible making simulation of the more complex Phase II system difficult and repeated simulations are tedious. A wave optics simulation written in IDL is more suitable. Initially we have used the IDL simulation to replicate the Stitch simulation of the Phase I system. In the future a more complete end-to-end simulation is desirable and we plan to extend the current IDL simulation to meet that need.

3. EFFECT OF AMPLITUDE VARIATION ON HIGH CONTRAST MEASUREMENTS

The method for measuring contrast in the far field on the ExAO testbed has been thoroughly described in previous works.[4,12] It is briefly outlined here. Typically far-field measurements are taken with a simple, single-opening prolate-spheroid-shaped pupil to suppress diffraction. The pupil is placed in front of the flat mirror or MEMS DM, and a focal plane mask is used either at focus 1 with the CCD right after or in the new system at focus position 1 with the CCD at focus position 2. The data in this section was all taken before the Phase II changes were implemented (and helped to motivate the change). A series of far-field images is taken with varying amounts of laser power to overcome the limited dynamic range of the camera. In the high-power images used to measure the wings of the PSF the focal plane block is used to block the core of the image, which would otherwise saturate the CCD. The shape of the PSF and focal plane mask result in a wedge shaped region of high contrast that has an angular size of between 4 and 8 degrees.

We demonstrated in 2006 that on the ExAO testbed, high-contrast measurements with a flat mirror were primarily limited by the uncorrected phase.[4] In that case we used the phase measured by the PSDI to simulate the far-field image and compared the simulation with the experimental result. The PSDI, however, measures both phase and amplitude, enabling us to return to that data set and do a second simulation. The results of the two simulations are compared to the experimental data in Fig. 2. From the new simulation it is clear that amplitude variations do play a role in limiting contrast in the flat mirror case outside of about 15 λ/D. In the case of high-contrast measurements with the MEMS the typical region of interest is a 4 degree wedge extending from 8 to 13 λ/D. The outer working distance is set by the spatial frequencies that can be controlled by the MEMS DM. In the flat mirror data this region is largely unaffected by systematic amplitude errors.

Unfortunately when the MEMS DM is added to the testbed amplitude errors increase, particularly over mid-spatial frequencies. The process for MEMS flattening, including an error budget is well described elsewhere,.[5] For these measurements the MEMS was flattened to 0.5 nm rms wavefront error within controllable spatial frequencies

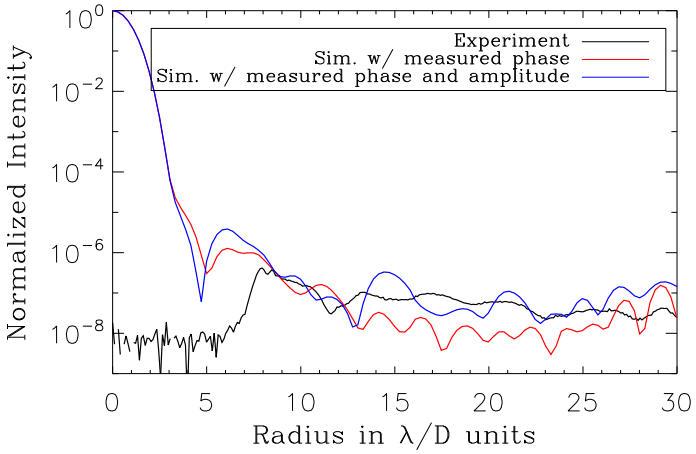

Figure 2. Radial average of experimentally measured contrast (using a flat mirror in place of DM and a prolate shaped pupil) is compared to a simulation from measured phase alone and measured phase and amplitude. Around 15 λ/D amplitude errors begin to limit contrast.

over the 9.2 mm aperture (measured in the MEMS plane). Figure 3 compares the experimentally measured contrast to the contrast simulated with the measured phase alone and the measured phase and amplitude, as was done in the flat mirror case. The inner working distance is set by bleeding from saturated areas on the CCD

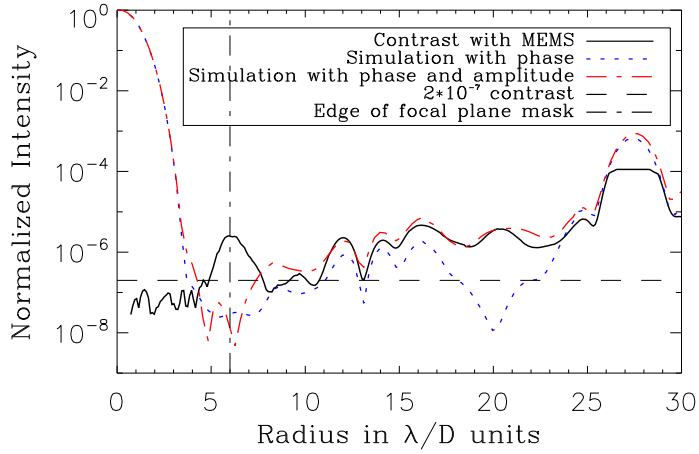

Figure 3. Radial average of experimental (with a shaped pupil) and simulated far-field images with the MEMS mirror. The black line is experimental MEMS data, the red line is a simulation with only phase and the blue line is a simulation using measured phase and amplitude. Clearly contrast is limited somewhat by amplitude errors, however the small region of high contrast makes it difficult to diagnose.

near the focal plane mask and in this region the simulations are also very sensitive to the exact placement of the shaped pupil mask. Examining the region of interest from 8 to 13 λ/D, it appears that the experimental result cannot be completely accounted for by the phase. It also appears that amplitude errors are overestimated by the PSDI. The limited region of diffraction suppression and wavefront control for this experiment make it difficult to diagnose the source of the error. Using the PSDI measurements we can simulate a more ideal case for diffraction suppression with a much larger region of high contrast. Figures 4 and 5 were simulated with a Blackman apodization. With a symmetric apodization we can radial average over the entire image and it is clear

that amplitude errors limit contrast a small but measurable amount over controllable spatial frequencies. In this case contrast is reduced by 3×10^{-7}, for comparison using a MEMS device with a window (to protect from humidity damage) will reduce contrast in our system by 1×10^{-7}. The dark hole region is not as noticeable as might be expected because of the relatively low out-of-band errors. There is an interesting difference between the two simulations for both the shaped pupil and Blackman apodization at 20 λ/D that was not seen in the flat mirror data.

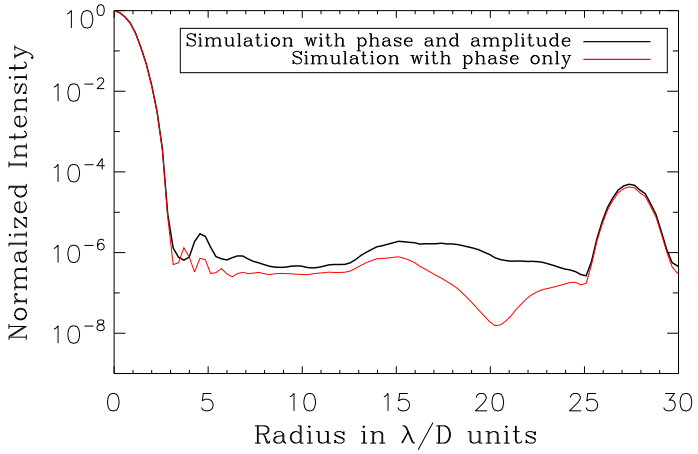

Figure 4. Radial average of PSF simulated with the measured phase alone and the measured phase and amplitude of the flattened MEMS DM, using a Blackman apodization for diffraction suppression. Amplitude variations appear to limit contrast by 3×10^{-7} over controllable spatial frequencies, and particularly at about 20 λ/D. The Blackman apodziation produces a larger region of high contrast, making amplitude effects easier to identify.

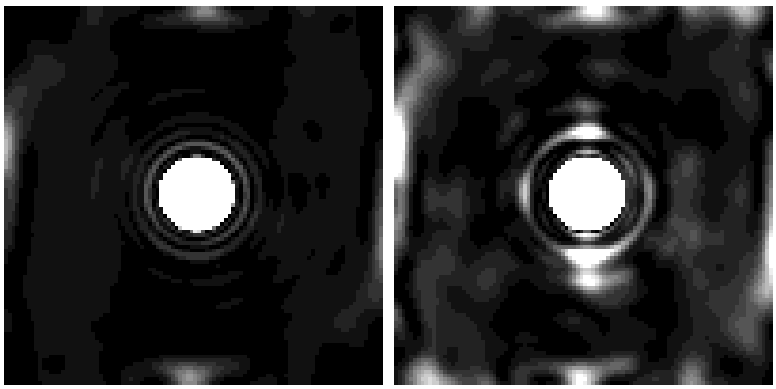

Figure 5. Simulated PSFs using the measured phase alone (left) and the measured phase and amplitude (right). These are shown on the same scale and approximate diameter of each is 27 λ/D, the 'dark hole' region.

From these comparisons it is clear that amplitude variations will potentially limit the contrast of the testbed, particularly when additional atmospheric-like abberations are included. The PSDI may be overestimating those errors making another means of measuring amplitude error desirable. It would also be much easier to understand the limitations of the far-field data if the region of high contrast was bigger. The Phase II system addresses these concerns. In particular the addition of an extra pupil and focal plane allows more sophisticated Lyot-style coronagraphs to be used, and the pupil imaging mode allows a more direct measurement of intensity variations in the system.

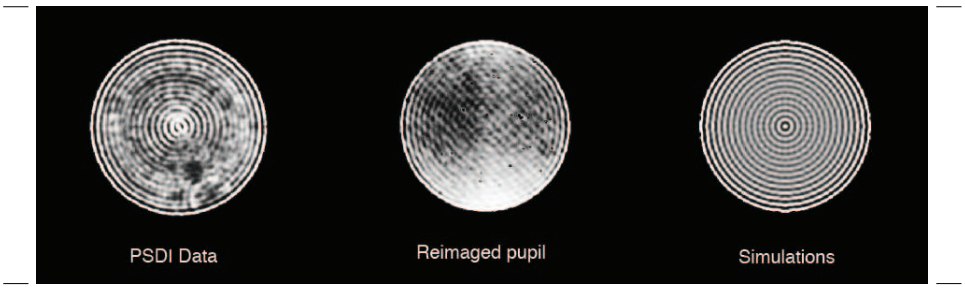

Figure 6. Intensity of the flat mirror measured in the pupil plane in pupil imaging mode (Lyot) and by the PSDI. The right image is an IDL simulation with uniform phase and amplitude, truncated as it propagates through focus.

4. SYSTEMATIC AMPLITUDE VARIATION

Systematic amplitude variations are measured with the flat mirror in place of the MEMS DM. The flat mirror for these measurements was aluminum coated, but we have since replaced it with a gold coated flat to correspond more closely to the MEMS. The intensity variations are measured using the PSDI and the new pupil imaging mode. Two sample images are shown in Fig. 6. The most obvious feature in the PSDI images is the ringing at the edges. This is also visible in phase measurements and in both cases is caused by truncation by an aperture located at the pinhole aligner (located at focus position 1 or 2). The ringing in the power spectrum provides a convenient feature for testing our simulation tools. Using both Stich and IDL to simulate a uniform phase and amplitude at the pupil plane, truncated by an aperture at the pinhole aligner we can reproduce the ringing seen in the power spectrum of the experimental data. The IDL simulated intensity is the right image in Fig. 6. The power spectra of the PSDI measured intensity, the pupil imaging mode intensity (also called Lyot mode because we are re-imaging the plane where the Lyot-stop goes) and the simple simulation using just uniform phase and amplitude are shown in Fig. 7. From the PSDI data the system has 2.2% intensity variation (calculated over a

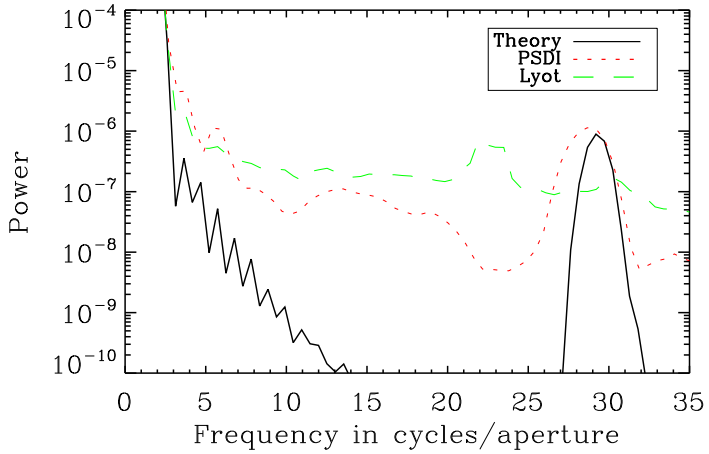

Figure 7. Power spectra corresponding to the three intensity images in Fig. 6. The peak at 30 cycles per aperture is caused by truncation at the pinhole. In pupil imaging mode fringing from the imaging CCD introduces error at just over 20 cycles per aperture.

75% aperture to avoid some of the ringing). Most of the error, 1.2%, is located from 0 to 5 cycles per aperture. These low-order errors are probably caused by non-uniform illumination. Without careful alignment of the input fiber these errors can be much bigger. Similar errors were measured at HCIT.[7] The pupil images have larger intensity variations, most likely caused by imperfections in the re-imaging optics and fringing produced by the

window of the imaging CCD. We are investigating better flat fielding or post-processing techniques to make the pupil imaging mode better. The fringing in the pupil image can also be seen as a small peak in the power spectrum in Fig. 7.

Another source of intensity variation in the system is phase and amplitude mixing. The system has low wavefront error, but it will be introduced from two different positions (the focusing lens and the flat mirror). Figure 8 is the power spectra of the original measured phase, a simulation using uniform phase and amplitude with the truncation at the pinhole aligner, and a simulation using uniform amplitude and the measured PSDI phase. The PSDI phase has been back propagated during acquisition so some errors may be magnified by the double propagation required for the simulation. The simulation indicates that phase errors can account for some, but not all of the amplitude variation seen in the PSDI measurement. The phase and amplitude mixing is more likely the source of higher order aberrations. This is consistent with the errors coming from the flat mirror in the system, which is 18 cm from the pupil plane. For example 20 cycles per aperture at a wavelength of 532 nm has a quarter talbot length (phase converts to positive amplitude) of about 23 cm?

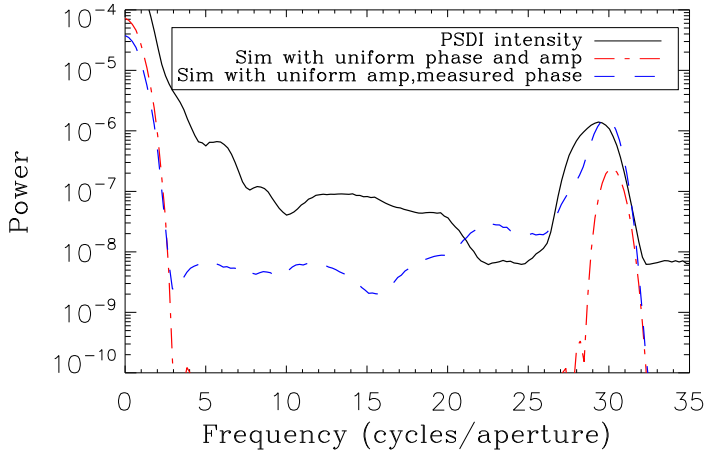

Figure 8. The power spectra of the measured PSDI intensity is compared with the intensity from a simulation using Stitch with uniform phase and amplitude (propagated to focus, truncated with the aperture of the pinhole aligner and then back to the pupil plane) and a similar simulation using uniform amplitude and the measured phase. Phase errors can account for some the of the intensity variation, but not all. The remaining error could be caused by real intensity variations introduced in the optical system.

Far-field simulations with the measured phase and amplitude for the flat mirror case correspond well with experimental results indicating that most of the measured amplitude errors are real. Some errors are introduced by truncation at the pinhole aligner or in the case of pupil imaging these can be introduced by the beam splitter used for the wavefront sensor. Phase and amplitude mixing might account for some errors, but not all of the measured error. The remaining error is probably caused by real intensity variations introduced by the optical system or other un-simulated wave-optic effects. The end-to-end simulation will help us confirm the source of mid-frequency error and the source of additional errors measured in the pupil imaging mode but not with the PSDI.

5. MEMS DM AMPLITUDE VARIATION

Based on the far-field measurements in Section 3 we know that the MEMS DM introduces amplitude variations which limit contrast. These errors could be caused by real variation in the reflectivity of the MEMS or could be caused by more complicated wave optic effects like phase and amplitude mixing. We are investigating both possibilities. Figure 9 is the PSDI measured intensity of the MEMS in the pupil plane and the MEMS plane. In the system with the flat mirror we see that there is some mixing at high spatial frequencies, but with the

introduction of more mid-frequency error with the MEMS device even minimal mixing can introduce measurable errors. Figure 10 is the power spectra of the measured intensity of the MEMS by the PSDI and in pupil imaging

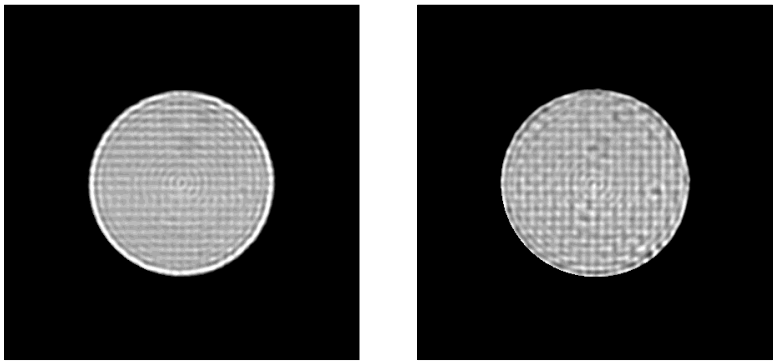

Figure 9. MEMS intensity measured by the PSDI in the MEMS plane (left) and the pupil plane (right). The pupil is separated from the MEMS plane by 18 cm.

mode, compared to the flat mirror. In this case all measurements are from the MEMS plane (the previous flat mirror power spectra are taken from the pupil plane). Based on the PSDI data the MEMS has 6 % rms intensity variation in the MEMS plane. Systematic low order intensity variations are still present and no worse with the introduction of the MEMS device (about 1.5 %). The peak at 22 cycles per aperture corresponds to the ripple on the MEMS device at the actuator spacing (for this data an 8 mm aperture was used) and accounts for another 2% rms error. The remaining mid-spatial frequency intensity errors introduced by the MEMS are significant and will interfere the most with far-field imaging. The mid-spatial frequency range in the MEMS intensity measured with the pupil imager is obscured probably by fringing from the CCD window, or errors in the re-imaging optics (the same problems noted with the flat mirror). We are investigating if these mid-frequency errors are caused by variations in reflectivity (see Section 5.1. The difference in intensity of the MEMS in the MEMS plane and

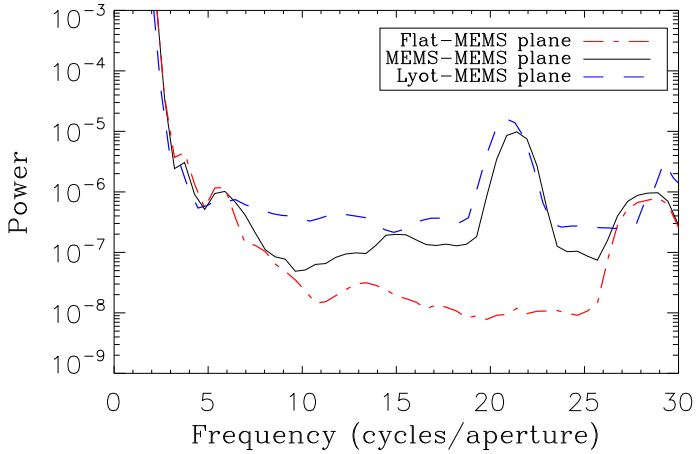

Figure 10. Power spectra of the MEMS intensity measured in pupil imaging mode and with the PSDI compared to the flat mirror. All measurements were made in the MEMS plane.

pupil plane can be seen in the images of Fig. 9 but the spatial frequency information from the power spectra of Fig. 11 is more useful. As expected there is not much amplitude and phase mixing at low spatial frequencies but a mid-spatial frequencies it is significant. From the PSDI intensity measured in the pupil plane the MEMS has 8% intensity variation with a significant amount in the mid-frequency range.

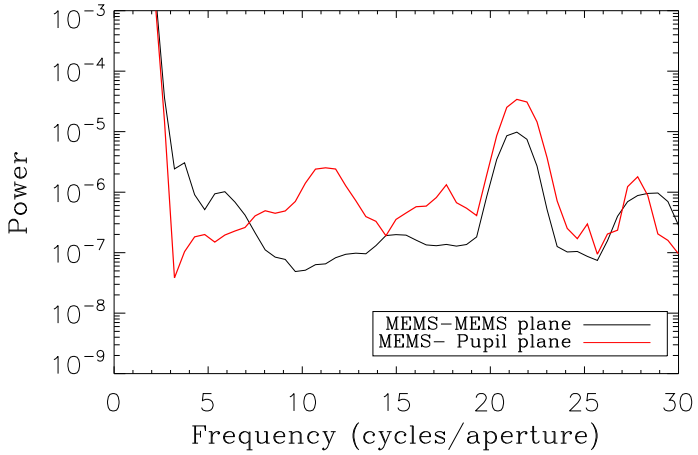

Figure 11. The power spectra of the MEMS intensity measured in the MEMS plane is compared to the intensity measured in the pupil plane. The changes in intensity between the MEMS and pupil plane are caused by phase and amplitude mixing.

One way to investigate the effect of phase on intensity is to introduce different wavefronts at the MEMS plane either in simulation or using the MEMS and then examine the effect at the pupil or MEMS plane. Ideally a phase placed at the MEMS plane and measured in the MEMS plane would not introduce any amplitude variation. The left and middle images in Figure 12 are an experimental measurement of the MEMS with a sinusoidal shape at the MEMS plane. The left image is the measured phase and the middle image is the measured intensity. On the right we have used Stitch to simulate introducing a uniform amplitude and a sinusoid in the phase at the MEMS plane. The wavefront was propagated to focus (and truncated) then propagated to the CCD and then back to the MEMS plane using the standard PSDI lensless imaging. In the IDL simulation (not shown here), which includes the truncation at the focus, but not the CCD, a phase introduced at the MEMS plane does not vary the amplitude in the re-propagated MEMS plane. This would seem to indicate that truncation at the CCD is responsible for the intensity variation, however the corresponding experimental pupil image is similar. We are still investigating these effects.

Figure 12. A sinusoid phase was introduced experimentally and in simulation at the MEMS plane. The left and middle images are the experimental PSDI measurements (phase and intensity respectively) of the MEMS plane after the shape was applied. On the right is the simulated intensity after a wavefront with uniform amplitude and sinusoid phase was propagated to the PSDI CCD and then back-propagated to the MEMS plane. Ideally there would no amplitude change in the this plane.

5.1 MEMS Reflectivity

From interferometry measurements we know that the MEMS has small scale structures, and those structures could affect the uniformity of the coating thickness and thereby change the reflectivity. Unfortunately the PSDI and the pupil imaging mode are both affected by wave-optic effects making an independent measurement of

MEMS reflectivity desirable. Measuring MEMS reflectivity over multiple points quantitatively has proven more difficult than we expected and we are continuing to explore other options.

A fiber-based spectrometer was used to measure the reflectivity of the MEMS relative to a Gold standard from Newport (ER.4). The MEMS was measured at multiple locations and an aluminum flat was also tested. It

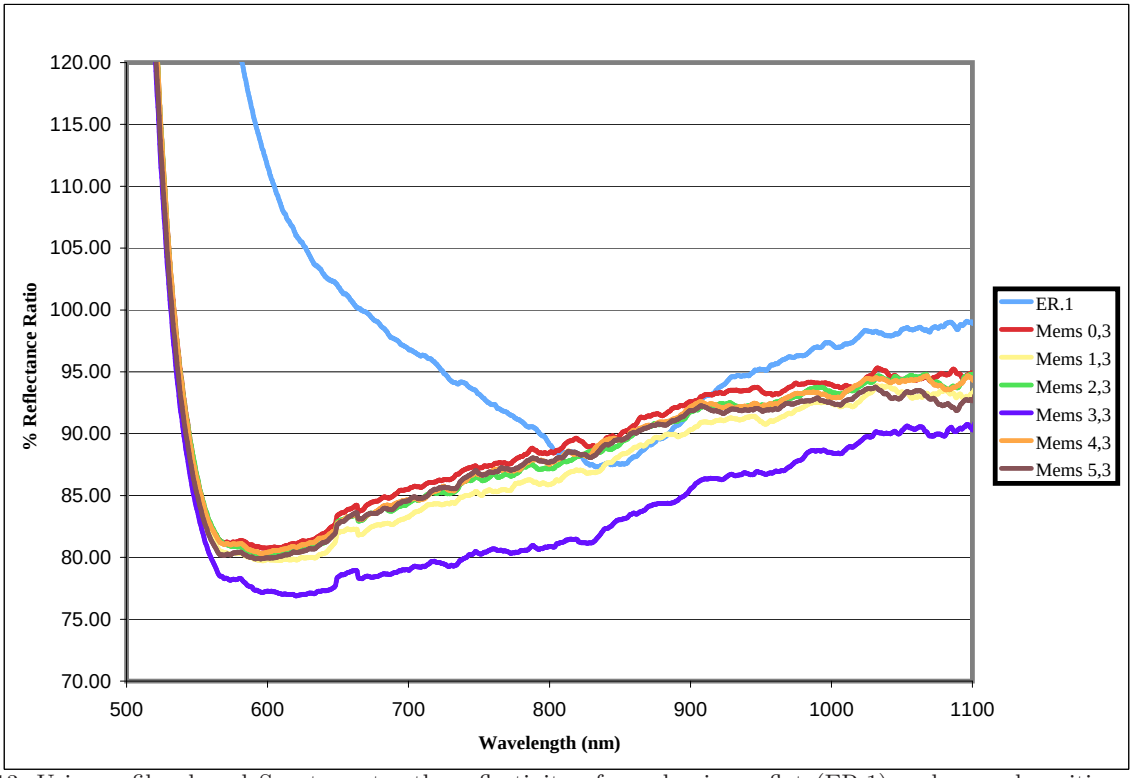

Figure 13. Using a fiber-based Spectrometer the reflectivity of an aluminum flat (ER.1) and several positions on the MEMS were relative to a Newport Gold Standard (ER.4). The gold standard has poor reflectivity at short wavelengths causing the spike in reflectivity ratio for the MEMS and aluminum flat below 550 nm. The testbed operates at 532 nm and as this chart indicates this is a poor wavelength for characterizing MEMS reflectivity. It appears that most areas of the MEMS are relatively uniform, but not all areas and even a variation of a few percent could be a problem.

is immediately clear from the results (See Fig. 13) that the 532 nm operating wavelength of the testbed is a poor choice for characterizing gold reflectivity. The gold standard has particularly poor reflectivity at less than 550 nm wavelengths causing even poor reflectivity of the MEMS at these wavelengths to have a high reflectivity ratio. As expected the aluminum flat is more much more reflective than the gold standard at short visible wavelengths. The variation between the MEMS positions indicates that even at higher wavelengths where the MEMS is more reflective there are variations in reflectivity, but absolute values and the resulting effect in the far-field are hard to quantify from these measurements (the MEMS positions were selected by moving the MEMS on a translation stage by hand). It is likely that a variation of even a few percent will introduce errors in the far field. A map of reflectivity across the device that could be used for simulations would be helpful. Testing the reflectivity of the MEMS at longer wavelengths will be investigated in the future.

Another way to examine MEMS reflectivity is to measure the thickness of the gold coating directly. The design of the DM calls for the gold to be 90 nm. We attempted to use a scanning electron microscope (SEM) in tunneling mode for this purpose. In this mode the ratio of gold and silicon can be compared at multiple positions. Measurements were taken from the four corners and twelve positions at 100 μm intervals from the center of a 140 actuator un-wired MEMS device. There was a variation in the ratio of gold to silicon of about 1%. This probably corresponds to a few percent variation in the thickness, which seems consistent with the fiber-based spectrometer data. The SEM can also be used to image the surface of the device. An SEM image of an etch hole on the test device is shown in Fig. 14.

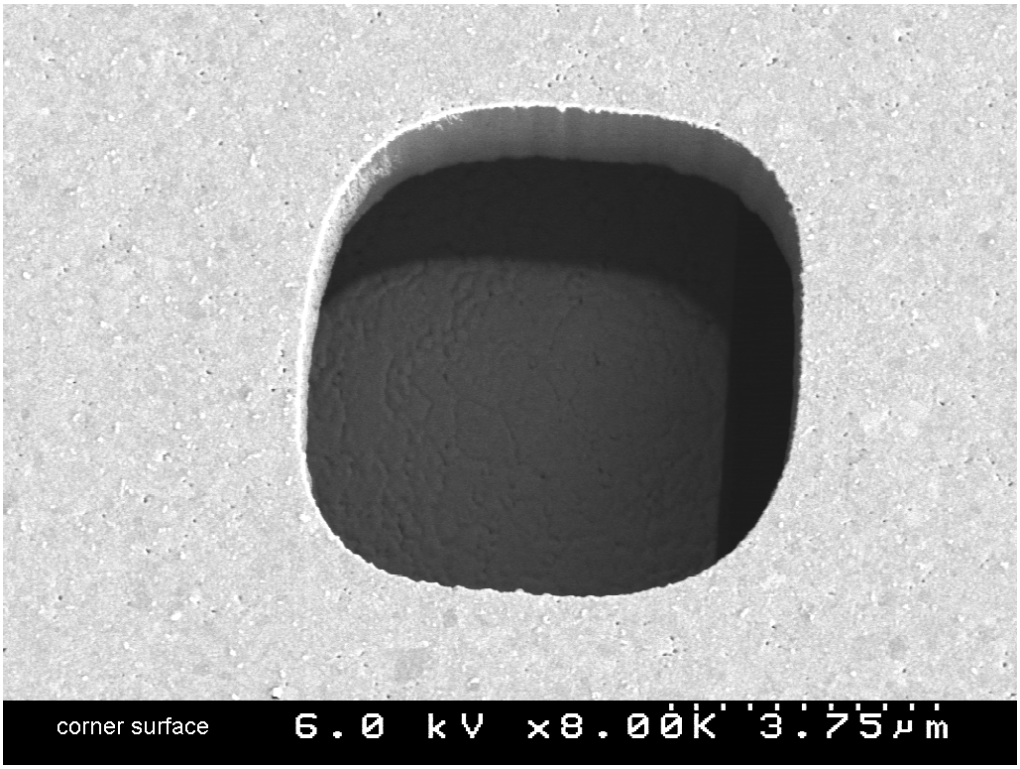

Figure 14. Scanning Electron Microscope of an etch hole on a sample 140 MEMS (no electrical connections). In Tunneling mode the SEM was used to estimate the thickness of the gold coating by comparing the ratio of gold to silicon. We estimate a uniformity in thickness of within a few percent.

6. CONCLUSIONS AND FUTURE WORK

Systematic amplitude variation on the ExAO testbed is about 2%, but when the MEMS is introduced to the system the error increases to 6% (8% when measured in the pupil plane). The amplitude errors introduced by the MEMS limit contrast a small but measurable amount. Some of the amplitude variation is caused by phase and amplitude mixing. This is a particular problem because the MEMS and the pupil plane are not conjugate. Other measurements of the MEMS device suggest that some intensity variation is caused by the non-uniform reflectivity of the MEMS device, which could be particularly problematic at the operating wavelength of the testbed because of the poor reflectivity of gold at the operating wavelength of 532 nm.

We will continue to investigate intensity variations in the system by developing an end-to-end simulation of the system. In particular we want to look at sinusoids of different spatial frequencies and their effect on the intensity at the pupil and MEMS planes. A full simulation of the far-field measurements with a lyot-style coronagraph would also help to understand the affect of amplitude variation on more realistic high-contrast measurements. We will also explore other methods for testing the MEMS reflectivity independently of the system including at longer wavelengths more like the GPI instrument.

ACKNOWLEDGMENTS

Contact Julia Evans at `evans74@llnl.gov`. The authors would like to acknowledge the assistance of Bryan Reed and Jim Ferreira for providing the scanning electron microscope data. This work has been supported in part by the Gordon and Betty Moore Foundation through its grant to the UCO/Lick Laboratory for Adaptive Optics and in part by the National Science Foundation Science and Technology Center for Adaptive Optics, managed by the University of California at Santa Cruz under cooperative agreement No. AST-9876783. This work was performed under the auspices of the U.S. Department of Energy by the University of California, Lawrence Livermore National Laboratory under contract No. W-7405-Eng-48.

REFERENCES

1. B. Macintosh, J. Graham, D. Palmer, R. Doyon, D. Gavel, J. Larkin, B. Oppenheimer, L. Saddlemyer, J. K. Wallace, B. Bauman, J. Evans, D. Erikson, K. Morzinksi, D. Phillion, L. Poyneer, A. Sivaramakrishnan, R. Soummer, S. Thibault, and J.-P. Veran, "The Gemini Planet Imager," in *Advances in Adaptive Optics II*, B. L. Ellerbroek and D. B. Calia, eds., *Proc. SPIE* **6272**, p. 62720L, 2006.
2. T. Fusco, G. Rousset, J. Sauvage, C. Petit, J. Beuzit, K. Dohlen, D. Mouillet, J. Charton, M. Nicolle, M. Kasper, *et al.*, "High-order adaptive optics requirements for direct detection of extrasolar planets: Application to the SPHERE instrument," *Optics Express* **14**(17), pp. 7515–7534, 2006.
3. J. Trauger and W. Traub, "A laboratory demonstration of the capability to image an Earth-like extrasolar planet.," *Nature* **446**(7137), pp. 771–3, 2007.
4. J. W. Evans, G. Sommargren, B. A. Macintosh, S. Severson, and D. Dillon, "Effect of wavefront error on 10^{-7} contrast measurements," *Optics Letters* **31 No.5**, pp. 565–567, 2006.
5. J. W. Evans, B. A. Macintosh, L. Poyneer, K. Morzinski, S. Severson, D. Dillon, D. Gavel, and L. Reza, "Demonstrating sub-nm closed loop MEMS flattening," *Optics Express* **14**, pp. 5558–5570, 2006.
6. S. Severson, B. Bauman, D. Dillon, J. Evans, D. Gavel, B. Macintosh, K. Morzinski, D. Palmer, and L. Poyneer, "The extreme adaptive optics testbed at UCSC: current results and coronagraphic upgrade," in *Advances in Adaptive Optics II*, D. B. C. Brent L. Ellerbroek, ed., *Proc. SPIE* **6272**, p. 62722J, 2006.
7. A. Lowman, J. Trauger, B. Gordon, J. Green, D. Moody, A. Niessner, and F. Shui, "High contrast imaging testebed for the terrestrial planet finder coronagraph," in *Optical, Infrared and Millimeter Space Telescopes*, J. C. Mather, ed., *Proc. SPIE* **5487**, pp. 1246–1254, 2003.
8. G. E. Sommargren, D. W. Phillion, M. A. Johnson, N. Q. Nguyen, A. Barty, F. J. Snell, D. R. Dillon, and L. S. Bradsher, "100-picometer interferometry for EUVL," in *Emerging Lithographic Technologies VI*, R. L. Engelstad, ed., *Proc. SPIE* **4688**, pp. 316–328, 2002.
9. L. A. Poyneer, B. Bauman, B. A. Macintosh, D. Dillon, and S. Severson, "Spatially filtered wave-front sensor for high-order adaptive optics," *Opt. Lett.* **31**, pp. 293–295, 2006.
10. C. Marois, D. Phillion, and B. Macintosh, "Exoplanet detection with simultaneous spectral differential imaging: effects of out-of-pupil-plane optical aberrations," in *Ground-based and Airborne Instrumentation for Astronomy*, Ground-based and A. I. for Astronomy, eds., *Proc. SPIE* **6269**, p. 62693M, 2006.
11. D. Phillion and G. Sommargren, "Point source diffraction interferometry with lensless imaging." presented at CfAO workshop on ExAO Calibration, October 2003.
12. J. W. Evans, K. Morzinski, L. Reza, S. Severson, L. Poyneer, B. Macintosh, D. Dillon, G. Sommargren, D. Palmer, D. Gavel, and S. Olivier, "Extreme adaptive optics testbed: High contrast measurements with a MEMS deformable mirror," in *Techniques and Instrumentation for Detection of Exoplanets II*, D. R. Coulter, ed., *Proc. SPIE* **5905**, pp. 303–310, 2005.